Comparison of Malta HF Radar Currents with CMEMS Mediterranean MFC Data

Georgios V. Kozyrakis[1][0000-0002-5896-6102], Andreas Nikolaidis[2,3][0000-0001-6214-8009],
Adam Gauci[4][0000-0001-8635-9230], George Zodiatis[2][0000-0003-2564-2686],
Joel Azzopardi[5][0000-0001-6709-8530], George Galanis[6][0000-0003-0620-9377],
Audrey Zammit[4][0000-0001-8777-5199], Sebastiano D'Amico[4][0000-0001-7429-4767],
George Alexandrakis[1][0000-0003-3690-3159], Vassiliki Metheniti[1][0000-0003-2154-5563],
Antonios Parasyris[1][0000-0001-9498-7245], Nikolaos A. Kampanis[1][0000-0001-6231-7730]

[1]Coastal & Marine Research Lab, Foundation for Research and Technology, N. Plastira 100,
Vassilika Vouton, GR-70013, Heraklion, Crete, Hellas
[2]ORION Research, Nicosia, Cyprus
[3]MARE INVESTIGATIORUM STUDIA (MIST) Ltd, Nicosia, Cyprus
[4]Department of Geosciences, Faculty of Science, University of Malta
[5]Department of AI, Faculty of ICT, University of Malta
[6]Hellenic Naval Academy Mathematical Modeling and Applications Lab, Athens, Hellas
gkoz@iacm.forth.gr

Abstract. This study evaluates hourly sea surface currents from the CALYPSO HF radar system against Copernicus CMEMS Med MFC data, covering the period from August 2022 to August 2023. The HF radar network, comprising four sites in Malta and three in Sicily, provides high-resolution, real-time surface current data. Results show that HF radar currents display greater temporal and spatial variability than the CMEMS data, primarily due to differences in spatial-temporal resolution. Notably, extreme current velocities differ between the datasets, with both indicating high values influenced by regional bathymetry. While HF radar data reflect currents at the very surface layer, CMEMS data correspond to a depth of 1.5 m. Nevertheless, after detrending and outlier removal, HF radar data align well with CMEMS Med MFC, especially in current direction. Both datasets depict a general anticyclonic circulation between northern Malta and southern Sicily. Periodic intensifications occur along the anticyclone's northern and southern edges. HF radar shows southeastward flow along Sicily's southern coast and opposing currents near Malta's northern coast. In contrast, CMEMS data indicate a stronger southeast flow along southern Sicily and generally weaker currents near Malta.

Keywords: sea-surface currents, high frequency radar, ocean remote sensing, Copernicus marine services data, statistical analysis.

1 Introduction

High-frequency (HF) radar systems have become indispensable tools in oceanography, particularly for monitoring sea-surface currents. These systems utilise radio waves to measure surface currents over broad spatial areas with high temporal resolution. Their utility has grown exponentially in recent years due to the increasing need for real-time oceanographic data to support maritime safety, pollution control, and climate change studies. The Mediterranean Sea, with its semi-enclosed nature and complex ocean dynamics, presents a unique environment for deploying and studying HF radar systems. This review synthesizes the current state of knowledge on the use of HF radar for observing sea-surface currents in the Mediterranean, focusing on technological principles, applications, and challenges.

The Mediterranean Sea's unique characteristics—including its semi-enclosed nature, high salinity, and complex bathymetry—make it a valuable region for studying sea-surface currents. HF radar installations have been deployed at several key locations to monitor oceanographic processes, such as: (i) the Ligurian Sea, where studies have focused on mesoscale eddies and their role in nutrient transport and primary production [1]; (ii) the Strait of Gibraltar, where HF radar data have been used to analyse the exchange of water masses between the Mediterranean and the Atlantic, providing insights into the hydrodynamic balance of the region [2]; and (iii) the Aegean and Adriatic Seas, where observations have highlighted the influence of river discharges, wind forcing, and seasonal variability on surface currents [3, 4]. Several European initiatives, such as EuroGOOS and the Copernicus Marine Service, have integrated HF radar data into broader ocean monitoring frameworks. These efforts have significantly enhanced our understanding of Mediterranean circulation patterns and their impact on marine ecosystems and human activities [5]. Other funded programs have also provide insights into the wave and current behaviour in the Mediterranean Sea. Specifically, HF radar systems in the Malta-Sicily Channel have been successfully validated for monitoring sea surface currents and wind waves. Studies confirm good agreement between radar-derived currents and independent data sources such as drifters, ADCPs, and models, particularly under low wind conditions. HF radar also shows potential for estimating wave height and period, with promising validation against buoy data [6-9].

HF radar data are frequently assimilated into numerical models to improve ocean forecasting [10]. Data assimilation techniques combine HF radar observations with model outputs to enhance predictions of current velocity, direction, and variability [2, 4, 11] Studies have demonstrated that assimilating HF radar data can significantly reduce forecast errors, particularly in regions with complex circulation patterns [12]. Validation efforts have also compared HF radar data with in-situ measurements from ADCPs, drifters, and satellite observations. These comparisons have highlighted both the strengths and limitations of HF radar systems, underscoring the need for continuous calibration and validation [13-15].

Despite their advantages, HF radar systems face several challenges, such as: (i) Signal interference: Electromagnetic interference from nearby radio systems can degrade data quality [16]; (ii) Environmental constraints: Rough seas and extreme weather conditions can reduce the range and accuracy of HF radar measurements [2, 17]; and (iii) Coastal dependence: HF radar installations are limited to coastal areas, leaving offshore regions less monitored [3, 5]. Addressing these challenges requires advances in hardware design, signal processing algorithms, and data assimilation techniques. Emerging technologies, such as machine learning, offer promising avenues for enhancing data interpretation and reducing uncertainty.

This manuscript is structured as follows. The Introduction provides a review of relevant literature and previous works on the subject. The Data Sources and Methodology section describes the sites, data acquisition methods and accompanying statistical framework used to generate the results. The Results and Discussion section presents the findings and includes comparisons with existing studies. The Conclusion summaries the current work and consider future trends and approaches. To streamline the presentation of results, key findings are consolidated in the Results and Discussion section with comprehensive data for the entire duration documented in the Appendix.

2 Data Sources and Methodology

HF radar systems operate by transmitting electromagnetic waves in the HF band (3–30 MHz) that interact with ocean surface waves. This interaction generates a phenomenon known as Bragg scattering, where radio waves are scattered back towards the radar at specific frequencies related to the speed and direction of surface currents. These measurements are then processed to produce real-time maps of sea-surface current velocity [1, 2]. Compared to alternative methods such as Acoustic Doppler Current Profilers (ADCPs) and satellite altimetry, HF radar systems offer unique advantages. They provide continuous, wide-area coverage (up to 200 km offshore) and high temporal resolution, making them ideal for monitoring dynamic and transient oceanographic phenomena [3]. However, the accuracy of HF radar systems can be influenced by environmental factors such as sea state, signal interference, and coastal topography [4].

2.1 Data Acquisition

In total, HF radar sea surface current data were analyzed for selected months in 2022 and 2023. For 2022, 744 hours of data were examined for August, October, and December, and 709 hours for September and November. In 2023, 744 hours were analyzed for January, March, May, July, and August; 709 hours for June; and 673 hours for February, while no reliable data were available for April. The study area spans latitudes 35.8°N to 37.0°N and longitudes 13.5°E to 15.3°E, encompassing the HF radar sampling locations (Figs. 1 and 2).

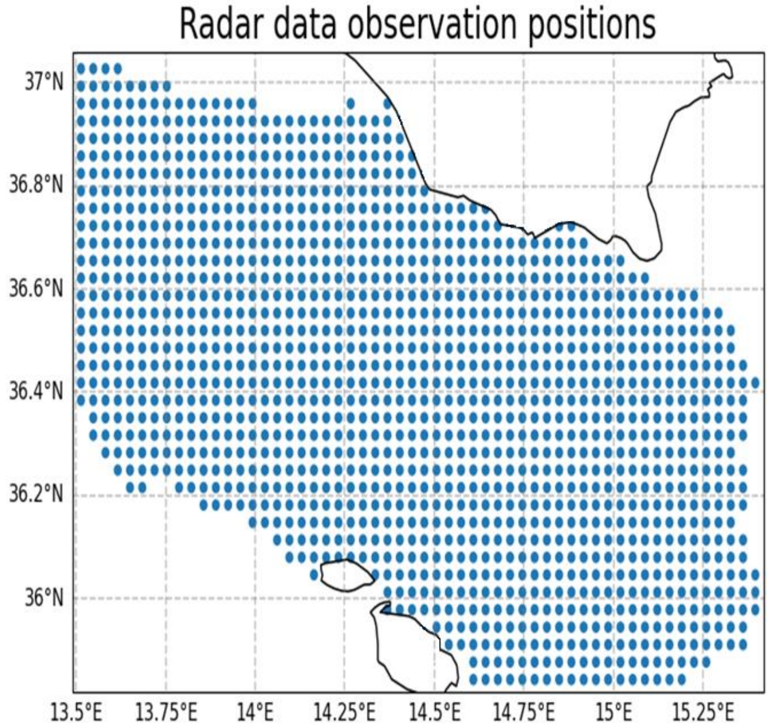

Fig. 1. Spatial coverage of the HF radar derived sea surface currents observational positions. Horizontal units: Decimal degrees (WGS84)

For the purpose of the HF radar data analysis, five HF radar sampling locations were selected, as shown in Table 1 and Fig. 2.

Table 1. Malta HF Radar sampling locations selected for analysis

Position	Longitude (°E)	Latitude (°N)
Point 1	14.5265881	36.5191649
Point 2	14.3264624	36.3564511
Point 3	14.7275500	36.5193336
Point 4	14.4925225	36.7083428
Point 5	14.4939845	36.2217168

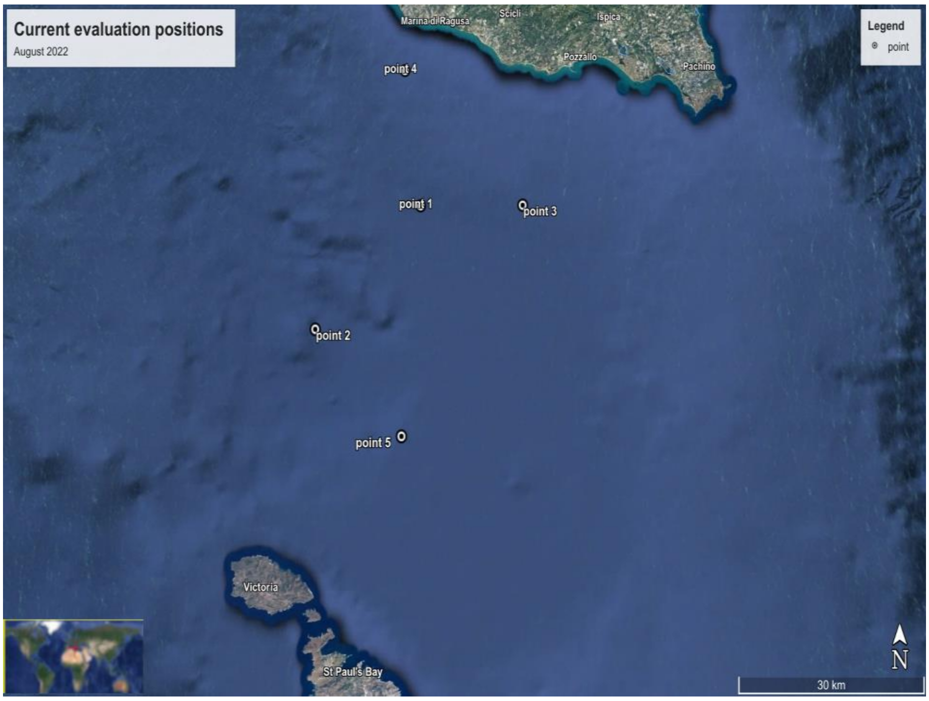

Fig. 2. The Malta 5 HF radar sampling locations used for the evaluation against the CMEMS Med MFC reanalysis data

The Malta HF radar U and V sea surface currents components, were compared with similar data obtained from the Copernicus Marine Portal product MEDSEA_ANALYSISFORECAST_PHY_006_013 [18] on a common grid. This is a near-real-time operational product from the CMEMS Med-MFC, which provides daily analysis (near-real-time with data assimilation), and 10-day forecasts of physical ocean parameters. It is generated using the EAS6 ocean model system and includes data assimilation of satellite and in situ observations. The Copernicus data are provided with an hourly time step. For the comparison purposes Copernicus data for the examined period were used. Missing values of HF Radar data were filled using linear interpolation. Time series of both, HF radar, and Copernicus data, were detrended using the moving average method over a window of two-hour window (two timesteps) in order to reduce short-term fluctuations and improve comparability between the two datasets. This window was selected to smooth high-frequency noise while preserving the underlying current patterns relevant to mesoscale circulation. A high-low pass filter was applied to smooth outlier data. The sea surface currents time series analysis includes data (in meters per second, m/s) from the Malta HF radar and Copernicus at the specified evaluation sampling locations every hour. The quantitative statistics performed included Root Mean Square Error (*RMSE*), Pearson product-moment correlation coefficient (*R*), Coefficient of Determination (R^2), Nash-Sutcliffe efficiency (*NSE*), Index of Agreement (*d*) and Percent Bias (*pbias*), as described in the following section.

2.2 Statistical Framework

A strong statistical framework has been created to back up the analysis mentioned above. The following error metrics, concisely summarised in Taylor's "Taylor Diagram" [19] and are the most frequently employed across various disciplines (for example, weather prediction, hydrology, etc.) where model and observation values have to be compared:

$$\boldsymbol{BIAS} = \frac{\mathbf{1}}{\boldsymbol{N}}\sum_{\boldsymbol{i=1}}^{\boldsymbol{N}}(\boldsymbol{P_i} - \boldsymbol{O_i}) = \overline{\boldsymbol{P}} - \overline{\boldsymbol{O}}, \tag{1}$$

$$\boldsymbol{PBIAS} = \frac{\sum_{\boldsymbol{i=1}}^{\boldsymbol{N}}(\boldsymbol{P_i} - \boldsymbol{O_i})}{\sum_{\boldsymbol{i=1}}^{\boldsymbol{N}}(\boldsymbol{O_i})} \times \mathbf{100}, \tag{2}$$

where ***N*** denotes the number of records, ***P*** the model prediction, and ***O*** the observation records. This statistical parameter provides information in a standard way about systematic errors, i.e., the tendency of the model to overestimate or underestimate the predicted values. BIAS serves as a measure of differences between observations and model data, with ideal values closer to zero. Note that bias can be positive or negative, indicating overprediction or underprediction.

$$\boldsymbol{RMSE} = \sqrt{\frac{\sum_{\boldsymbol{i=1}}^{\boldsymbol{N}}(\boldsymbol{P_i} - \boldsymbol{O_i})^2}{\boldsymbol{N}}}. \tag{3}$$

RMSE (Root Mean Squared Error), is utilized as a measure of the variability of the error and offers an indication of the efficacy of the model to predict the general behaviour of the system. Ideal value is 0, and the lower the value, the better the model performance [20].

The ***Nash-Sutcliffe model efficiency coefficient*** [21], defined as follows:

$$\boldsymbol{NS} = \mathbf{1} - \frac{\sum_{\boldsymbol{i=1}}^{\boldsymbol{N}}(\boldsymbol{O_i} - \boldsymbol{M_i})^2}{\sum_{\boldsymbol{i=1}}^{\boldsymbol{N}}(\boldsymbol{O_i} - \overline{\boldsymbol{O}})^2}. \tag{4}$$

The values of this parameter vary from -∞ to 1, where 1 indicates the perfect match between observations and model data. A zero value suggests that the accuracy of the model is as good as the accuracy of the mean observational value.

The ***Correlation Coefficient***: see for example [19,20]

$$\boldsymbol{r} = \frac{\sum_{\boldsymbol{i=1}}^{\boldsymbol{N}}((\boldsymbol{x_i} - \overline{\boldsymbol{x}})(\boldsymbol{y_i} - \overline{\boldsymbol{y}}))}{(\sum_{\boldsymbol{i=1}}^{\boldsymbol{N}}(\boldsymbol{x_i} - \overline{\boldsymbol{x}})^2 \sum_{\boldsymbol{i=1}}^{\boldsymbol{N}}(\boldsymbol{y_i} - \overline{\boldsymbol{y}})^2)^{\frac{\mathbf{1}}{\mathbf{2}}}}, \tag{5}$$

which measures the linear correlation between forecasts (y_i) and observations (x_i), and takes values lower or equal to 1 with higher values indicating stronger correlation.

Coefficient of Determination (R^2): The coefficient of determination represents the proportion of variance in the dependent variable that is predictable from the independent variable. It is the square of the Pearson correlation coefficient (R).

The **Index of Agreement** (***d***) is a statistical measure used to evaluate the goodness of fit between observed and predicted values, widely employed to assess how well a model's results match the observed data. It ranges from 0 to 1, where 1 represents perfect agreement, and 0 represents no agreement. The formula for the Index of Agreement (d) is:

$$d = 1 - \frac{\sum_{i=1}^{n}(O_i - P_i)^2}{\sum_{i=1}^{n}\left(\left|O_i - \overline{O}\right| + \left|P_i - \overline{O}\right|\right)^2}, \tag{6}$$

where O_i is the observed value for the i-th observation, P_i is the predicted value for the i-th observation, $\overline{O}$ is the mean of the observed values, $\overline{P}$ is the mean of the predicted values and n is the number of observations.

For $d = 1$, perfect agreement between observed and predicted values is established. For $d = 0$ there is no agreement (meaning predictions are entirely off from observations) and $d < 1$ is the lower the value of d, the worse the agreement between observed and predicted values. The index of agreement differs from R^2, because R^2 reflects how well the model explains the variance in the data, whereas d reflects how closely the predicted values match the observed values, regardless of the variance.

3 Results and Discussion

Table 2 to Table 6 present the statistical metrics assessing the performance of current speed predictions for Points 1 to 5 across different months. Regarding the RMSE trends.

RMSE values remain relatively low (0.02 to 0.07) across all points, indicating minor errors in prediction. The lowest RMSE occurs in March to May 2023 across multiple points, suggesting better predictive accuracy in those months. The highest RMSE is observed in December 2022 and February 2023, likely due to seasonal variations affecting water currents. For the Coefficient of Determination (R^2), October 2022, August 2023, and May 2023 generally exhibit the highest R^2 values, indicating better model performance in these months. June 2023 and November 2022 show the lowest R^2 values across multiple points, meaning the model explains very little variance in the observed data. Regarding the results on percent bias, high positive PBIAS (> 100%) in February 2023 (Point 1, Point 5) and July 2023 (Point 1) indicates the model is overestimating current speed. High negative PBIAS (< -50%) in December 2022 and June 2023 (Points 1, 2, 3, 4, 5) suggests significant underestimation. For Nash-Sutcliffe Efficiency coefficient (NSE), the best months in terms of NSE are May 2023, October 2022, and August 2023 across multiple points. The worst months (NSE < 0, meaning worse than a simple mean predictor) are February 2023, June 2023, and December 2022, suggesting the model fails in those months. For the Index of Agreement (d) and Correlation Coefficient (R), the highest agreement (d > 0.60) and correlation (R > 0.60) appear in August 2023, October 2022, and May 2023, indicating better alignment between predictions and observations. Weak correlation (R < 0.3) and agreement (d < 0.4) are observed in June 2023, November 2022, and February 2023 across multiple points.

All statistical indexes are reported in Tables 2 to 6 for each point and the summary Table 7 is highlighting the "best-performing" and "worst-performing" months across all locations.

There are apparent seasonal trends in the timeseries where, winter months (December - February) generally show poor model performance with negative NSE and extreme biases. Spring and summer months (May to August) exhibit better results, particularly in terms of correlation and agreement. Overall, the best performing month is May 2023 since across multiple points, it has high R^2, positive NSE, and strong agreement and the worst performing month is February 2023 with extreme bias, low NSE, poor correlation across most points. These results are better visualized in the monthly Taylor diagrams in Fig. 9.

Table 2. Current speed statistical indexes for Point 1

Point 1	***RMSE***	***R^2***	***PBIAS***	***NSE***	***d***	***R***
August 2022	0.06	0.15	32.80	-0.01	0.29	0.56
September 2022	0.05	0.31	-6.60	0.09	0.42	0.61
October 2022	0.05	0.30	-3.80	0.08	0.39	0.57
November 2022	0.06	0.06	-3.10	0.05	0.36	0.24
December 2022	0.07	0.26	-58.90	0.07	0.32	0.63
January 2023	0.05	0.24	-38.50	0.06	0.33	0.60
February 2023	0.04	0.16	132.10	-0.17	0.38	0.52
March 2023	0.02	0.31	12.40	-0.17	0.57	0.42
May 2023	0.03	0.40	-12.80	0.12	0.60	0.54
June 2023	0.03	0.00	-105.70	-0.27	0.38	0.06
July 2023	0.03	0.11	132.40	-0.23	0.34	0.48
August 2023	0.04	0.48	33.8	0.1	0.67	0.61

Table 3. Current speed statistical indexes for Point 2

Point 2	***RMSE***	***R^2***	***PBIAS***	***NSE***	***d***	***R***
August 2022	0.04	0.1	-24.4	-0.02	0.25	0.53
September 2022	0.04	0.13	-56	-0.03	0.31	0.58
October 2022	0.03	0.31	-61.7	0.1	0.37	0.61
November 2022	0.04	0.05	-71.1	0.05	0.3	0.23
December 2022	0.05	0.04	11.5	-0.02	0.18	0.61
January 2023	0.06	0.18	-7.4	0.01	0.28	0.61
February 2023	0.05	0.04	-65	-0.03	0.17	0.6
March 2023	0.04	0.08	-59.6	-0.05	0.28	0.61
May 2023	0.03	0.11	-29.5	-0.06	0.31	0.53
June 2023	0.03	0	-62	-0.2	0.38	0.06
July 2023	0.04	0.26	-44.6	0.06	0.35	0.64
August 2023	0.05	0.29	-28.5	0.08	0.39	0.62

Table 4. Current speed statistical indexes for Point 3

Point 3	***RMSE***	***R^2***	***PBIAS***	***NSE***	***d***	***R***
August 2022	0.03	0.28	4.90	-0.05	0.52	0.43
September 2022	0.03	0.36	-17.20	0.12	0.50	0.56
October 2022	0.03	0.47	2.70	0.21	0.61	0.61
November 2022	0.04	0.04	-43.70	-0.03	0.41	0.20
December 2022	0.03	0.39	-62.00	0.15	0.51	0.61
January 2023	0.04	0.19	-49.00	-0.05	0.39	0.56
February 2023	0.04	0.24	-17.90	0.04	0.41	0.60
March 2023	0.03	0.33	49.40	-0.10	0.58	0.46
May 2023	0.03	0.28	-23.50	0.02	0.48	0.53
June 2023	0.03	0.05	-65.90	-0.03	0.46	0.22
July 2023	0.04	0.12	77.10	0.18	0.34	0.58
August 2023	0.04	0.33	45.90	0.03	0.52	0.60

Table 5. Current speed statistical indexes for Point 4

Point 4	**RMSE**	**R2**	**PBIAS**	**NSE**	**d**	**R**
August 2022	0.02	0.25	-44.00	-0.02	0.50	0.35
September 2022	0.02	0.23	-61.10	-0.01	0.47	0.51
October 2022	0.02	0.28	-55.50	0.03	0.50	0.41
November 2022	0.03	0.10	-61.40	0.07	0.52	0.32
December 2022	0.03	0.31	-79.60	0.07	0.48	0.54
January 2023	0.04	0.12	-77.30	-0.02	0.28	0.57
February 2023	0.05	0.10	-20.70	-0.12	0.29	0.54
March 2023	0.04	0.12	93.00	-0.04	0.33	0.58
May 2023	0.03	0.10	133.30	-0.17	0.36	0.51
June 2023	0.03	0.01	-110.10	-0.14	0.39	0.11
July 2023	0.04	0.15	42.30	-0.04	0.34	0.57
August 2023	0.04	0.27	-8.20	0.02	0.47	0.58

Table 6. Current speed statistical indexes for Point 5

Point 5	***RMSE***	***R^2***	***PBIAS***	***NSE***	***d***	***R***
August 2022	0.03	0.24	-43.10	0.04	0.40	0.54
September 2022	0.03	0.18	-35.70	0.01	0.35	0.57
October 2022	0.07	0.07	-56.90	0.00	0.13	0.64
November 2022	0.03	0.19	-69.20	0.18	0.49	0.44
December 2022	0.04	-0.01	-74.80	-0.04	0.15	0.58
January 2023	0.06	0.14	-31.70	0.01	0.26	0.61
February 2023	0.06	0.05	321.90	-0.04	0.15	0.62
March 2023	0.05	0.09	-64.80	0.00	0.18	0.63
May 2023	0.03	0.24	-35.70	0.03	0.40	0.55
June 2023	0.03	0.00	-98.00	-0.14	0.30	0.01
July 2023	0.03	0.28	-32.80	0.08	0.42	0.60
August 2023	0.04	0.29	-26.60	0.08	0.41	0.62

Table 7. Summary table highlighting “best-performing” and “worst-performing” months across all locations

Point	**Best-Performing Months**	**Worst-Performing Months**	**Performance Indicators**
Point 1	May 2023, August 2023	February 2023, June 2023	High R^2, low RMSE, positive NSE; vs. negative NSE, extreme PBIAS, weak corr.
Point 2	July 2023, August 2023, October 2022	December 2022, February 2023, June 2023	Better R^2, moderate RMSE; vs. low R^2, high negative PBIAS
Point 3	October 2022, December 2022, August 2023	November 2022, June 2023	High R^2, strong agreement; vs. low NSE, weak correlation
Point 4	August 2023, November 2022	June 2023, May 2023	Higher R^2, moderate RMSE; vs. extreme negative PBIAS, weak correlation
Point 5	May 2023, August 2023, July 2023	February 2023, June 2023	Good R^2, moderate RMSE, positive NSE; vs. low R^2, high PBIAS, negative NSE

Figs. 3 to 7 compare data from the two sources, "HF radar data" (in red) and "MFC data" (in black) over the specific period for two characteristic months per location 1 to 5. Both datasets exhibit a consistent trend over time, suggesting they generally align in capturing the current-speed distribution. Variability in the radar data is significantly higher, with extreme peaks and troughs compared to the relatively stable MFC data. The radar data shows high-frequency variability, with frequent extreme outliers both above and below the mean. This is due to the sensitivity of the HF radar system to transient changes in measurement. The MFC data shows much smoother distribution, implying lower variability and a more generalised and filtered dataset, as it is expected from a analysis-type dataset. The variability of radar data captures real transient events (e.g., rapid current shifts) and is more suitable for short-term event detection compared to the MFC. The quantitative validation (RMSE, R^2, bias, etc.) between the two datasets that was previously presented confirms their agreement and highlights the specific discrepancies.

More specifically in Fig. 3 (Point 1 – October 2022 & May 2023) the comparison reveals stronger agreement between HF radar and CMEMS analysis data in May 2023, as evidenced by similar patterns and magnitudes in current speed over time. October 2022 shows more divergence, with HF radar capturing higher variability and peak values not reflected in the CMEMS data, suggesting potential surface-layer dynamics or finer temporal resolution in the radar measurements. In both months in Fig. 4 (Point 2 – November 2022 & March 2023), general trends in current speed align reasonably well between datasets, although the radar data in March 2023 shows higher short-term variability. November 2022 presents more stable and synchronized behavior, indicating better performance in moderate oceanographic conditions. Discrepancies may reflect localized wind effects or resolution differences. In Fig. 5 (Point 3 – September 2022 & February 2023) a stronger mismatch is observed in February 2023, where HF radar indicates pronounced peaks and variability not captured by the CMEMS analysis model data, potentially due to wind-driven surface currents. September 2022 shows better alignment in magnitude and phase, although radar data still appears more dynamic, possibly highlighting radar's sensitivity to transient features. In Fig. 6 (Point 4 – December 2022 & July 2023) July 2023 demonstrates good agreement in both trend and amplitude, with radar and CMEMS curves closely following one another. In contrast, December 2022 reveals noticeable divergence, with HF radar showing greater fluctuation and occasional overestimation, which may indicate limitations in model representation during winter conditions or increased radar noise. In Fig. 7 (Point 5 – August 2022 & March 2023) August 2022 exhibits strong correlation and minimal deviation between the two datasets, indicating robust model performance under summer conditions. In March 2023, while the general trend is preserved, HF radar data exhibits more short-term variability and slightly higher peak speeds, consistent with expected near-surface turbulence effects not fully resolved by CMEMS at 1.5 m depth.

The observed differences in sea surface current velocities between HF radar and Copernicus data can be partially attributed to the measurement depth. HF radar captures surface currents in the top few decimeters of the ocean, where wind forcing and surface turbulence are more pronounced. In contrast, the Copernicus model provides data at 1.5 m depth, where the direct influence of wind is reduced due to vertical shear and frictional effects. Previous studies (e.g., [22], [23]) have demonstrated that surface-layer currents can differ significantly from those even slightly below the surface, especially under strong wind or wave conditions. Therefore, differences between the two datasets are expected and consistent with physical oceanographic principles. In order to make the presentation of the results more compact, the results for the total duration period are documented in the Appendix (Fig. Ap1 to Fig. Ap5).

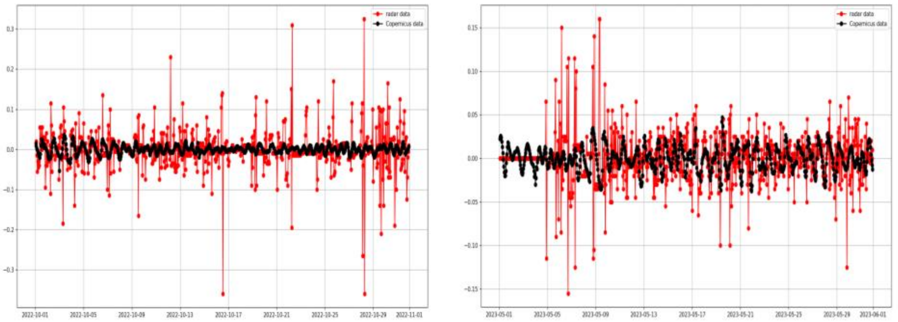

Fig. 3. Current speed temporal distribution from Radar HF data (red line) versus CMEMS Med MFC data (black line) for Point 1 for two characteristic months: October 2022 (left) and May 2023 (right)

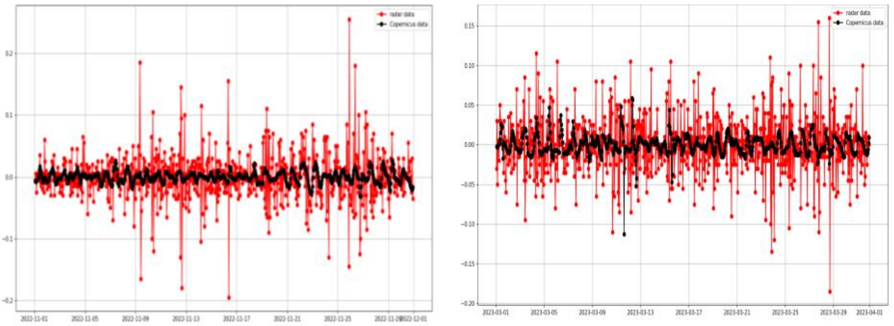

Fig. 4. Current speed temporal distribution from Radar HF data (red line) versus CMEMS Med MFC data (black line) for Point 2 for two characteristic months: November 2022 (left) and March 2023 (right)

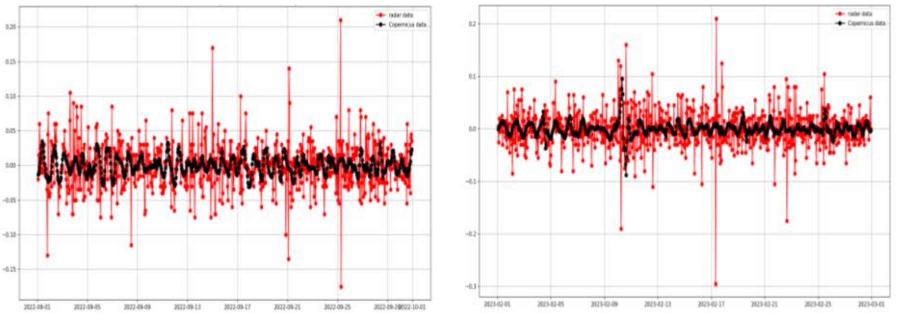

Fig. 5. Current speed temporal distribution from Radar HF data (red line) versus CMEMS Med MFC data (black line) for Point 3 for two characteristic months: September 2022 (left) and February 2023 (right)

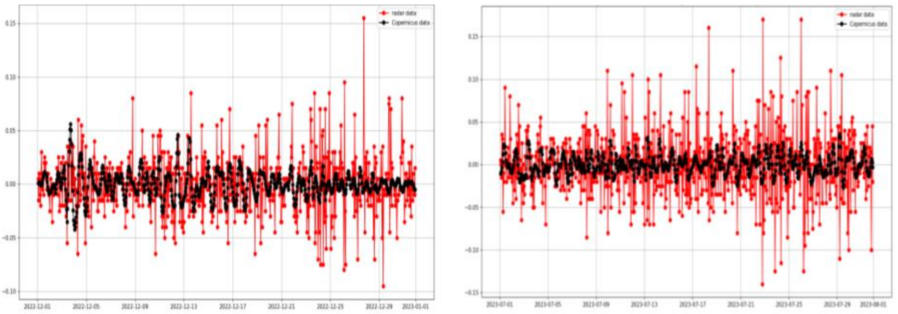

Fig. 6. Current speed temporal distribution from Radar HF data (red line) versus CMEMS Med MFC data (black line) for Point 4 for two characteristic months: December 2022 (left) and July 2023 (right)

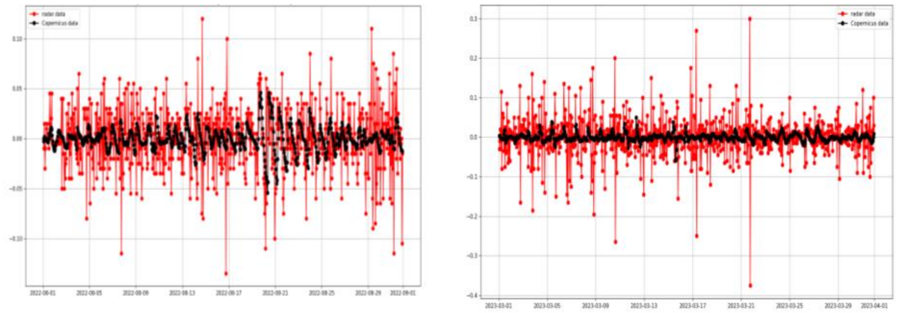

Fig. 7. Current speed temporal distribution from Radar HF data (red line) versus CMEMS Med MFC data (black line) for Point 5 for two characteristic months: August 2022 (left) and March 2023 (right)

The overall distribution of the vector plots (Fig. 8) for the entire region of interest, shows similarities with the HF-radar data being much more detailed, displaying open-sea recirculation patterns and specific current paths in the region. The plots in Fig. 8 are given for selected timeframe (2022-09-15 12:00 UTC). Characteristic results for the total duration over the period from August 2022 to August 2023 are documented in the Appendix (Fig. Ap6).

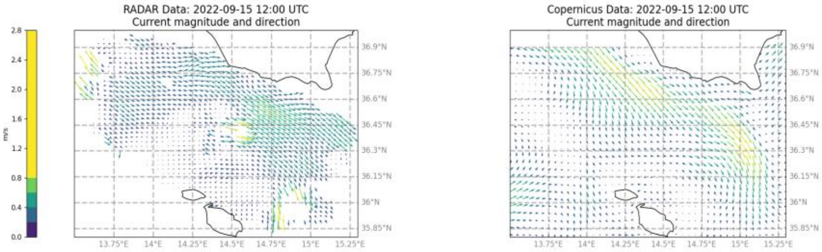

Fig. 8. Characteristic spatial distribution of current speed and direction from Radar HF data (left) versus CMEMS Med MFC data (right) at a specific time-point (2022-09-15 12:00 UTC) based on the entire spatial coverage of the HF radar (shown in Fig. 1). Horizontal units: Decimal degrees (WGS84)

The Taylor diagram in Fig. 9 visualises the monthly distribution results in Table 2 to Table 6. In general, the results agree well between the HF-radar and MFC data with diminished RMSE and standard deviation indexes. The MFC data indexes are clustered in a tight box for all locations throughout the year. Each dot represents a different month, characterized by its correlation coefficient, standard deviation, and centered root mean square error (RMSE) relative to the radar observations (black star). Across all points, several general trends emerge. High-performing months (e.g., August 2023, May 2023, July 2023) are located closer to the reference star, indicating strong correlations (often above 0.8), well-matched variability (standard deviation close to observed) and low RMSE, indicating strong agreement between observed and modelled current speeds. Poor-performing months such as February 2023 and June 2023 are located farther from the reference, show low correlation (some below 0.4), deviate in standard deviation (either under- or overestimated) and reflect high RMSE, pointing to limited model skill during these periods. More specifically, points P1 & P3 show better overall agreement, with most months clustering tightly near the observation reference. P2 & P4 display greater spread, suggesting more variability in model performance. P5 shows generally good agreement, with February and June again standing out as poor months. These results underscore the seasonal and spatial variability in model performance, with summer months generally aligning better with HF radar data and winter or transition months exhibiting reduced comparison, likely due to more complex or transient oceanographic processes not fully captured by the model.

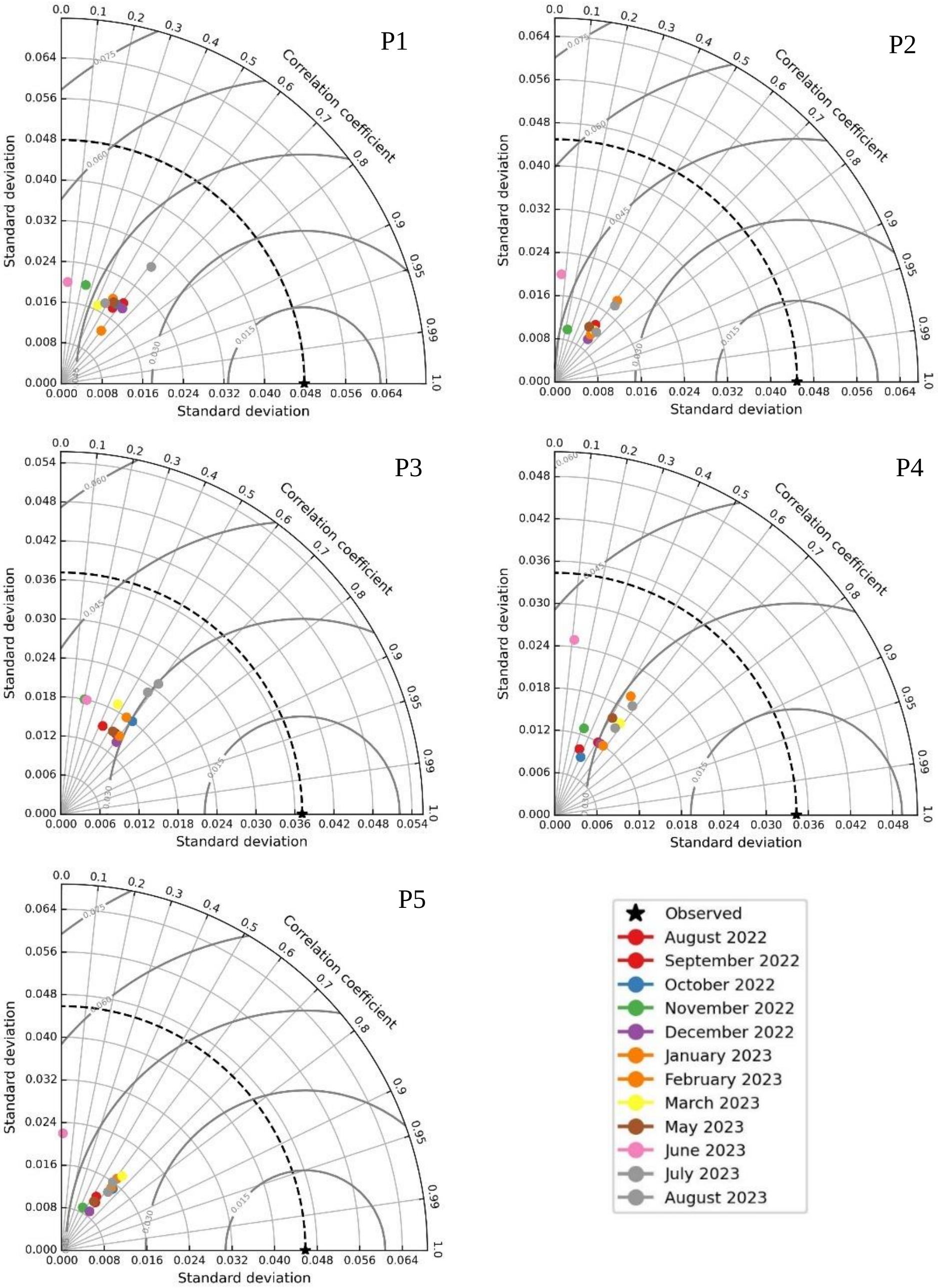

Fig. 9. Taylor diagrams of monthly current speed from Radar HF data (observed) versus CMEMS Med MFC data (colored dots) for positions P1 – P5

4 Conclusions

The detrended HF radar sea-surface current data, excluding outliers, align well with the CMEMS Med MFC analysis model data. Overall, the best performing month is May 2023 since across multiple points, it has high R^2 and positive NSE. The worst performing month is February 2023 with extreme bias, low NSE, and poor correlation across most points. The direction of the sea-surface currents between the two datasets is also in good agreement. The CMEMS Med MFC shows a strong south-east flow along Sicily's southern coastline, while the sea-surface currents along the northern Maltese coastline are generally weak. To address model–data discrepancies, future work will focus on several complementary strategies. Firstly, enhanced temporal and spatial harmonization between HF radar observations (which measure surface currents) and model output (at ~1.5 m depth) can be achieved by incorporating vertical current structure profiles from in-situ measurements or high-resolution 3D numerical models. Secondly, data assimilation techniques that integrate real-time HF radar measurements into hydrodynamic models could significantly improve predictive accuracy. Additionally, expanding the HF radar network—particularly in under-sampled coastal and transitional zones—would improve spatial coverage and resolve fine-scale circulation features. Coupling radar observations with wind forcing and wave models may help disentangle external drivers of surface current variability, ultimately strengthening both operational and scientific utility of such integrated observing systems.

The future of HF radar technology in the Mediterranean lies in expanding its spatial coverage and integrating it with other observational platforms. Innovations in radar design and data processing, coupled with international collaborations, can further enhance the utility of HF radar systems for monitoring and managing Mediterranean marine environments. Additionally, the incorporation of HF radar data into global oceanographic models can provide more accurate and comprehensive insights into ocean dynamics. HF radar systems have revolutionized our ability to monitor sea-surface currents, offering unparalleled spatial and temporal resolution. In the Mediterranean Sea, these systems have provided valuable insights into regional circulation patterns and their implications for marine ecosystems, climate studies, and human activities. While challenges remain, ongoing technological advancements and collaborative efforts promise to unlock the full potential of HF radar for oceanographic research and practical applications.

Acknowledgements

The authors acknowledge the financial support of the i-waveNET project "Implementazione di un sistema innovativo di monitoraggio dello stato del mare in scenari di cambiamento climatico", cod. C2 3.2 106, Program INTERREG V A Italia-Malta 2014 2020 (Interreg V-A Cross Border Cooperation Italia–Malta projects).

References

1. Paduan, J.D. and L.K. Rosenfeld, Remotely sensed surface currents in Monterey Bay from shore-based HF radar (Coastal Ocean Dynamics Application Radar). 1996. 101(C9): p. 20669-20686
2. Chapman, R.D., et al., On the accuracy of HF radar surface current measurements: Intercomparisons with ship-based sensors. 1997. 102(C8): p. 18737-18748
3. Graber, H.C., D.R. Thompson, and R.E. Carande, Ocean surface features and currents measured with synthetic aperture radar interferometry and HF radar. Journal of Geophysical Research: Oceans, 1996. 101(C11): p. 25813-25832
4. Hernandez-Lasheras, J., et al., Evaluating high-frequency radar data assimilation impact in coastal ocean operational modelling. Ocean Sci., 2021. 17(4): p. 1157-1175
5. Rubio, A., et al., HF Radar Activity in European Coastal Seas: Next Steps toward a Pan-European HF Radar Network. 2017. 4
6. Roarty, H., et al., The Global High Frequency Radar Network. 2019. Volume 6 - 2019.
7. Orasi, A., et al., HF radar for wind waves measurements in the Malta-Sicily Channel. Measurement, 2018. 128: p. 446-454
8. Drago, A., et al., Sea Surface Currents by HF Radar in the Malta Channel. 2013.
9. Capodici, F., et al., Validation of HF radar sea surface currents in the Malta-Sicily Channel. Remote Sensing of Environment, 2019. 225: p. 65-76
10. He, S., et al., Quality Control for Ocean Current Measurement Using High-Frequency Direction-Finding Radar. 2023. 15(23): p. 5553
11. Frolov, S., et al., Improved statistical prediction of surface currents based on historic HF-radar observations. Ocean Dynamics, 2012. 62(7): p. 1111-1122
12. Breivik, Ø. and Ø. Sætra, Real time assimilation of HF radar currents into a coastal ocean model. Journal of Marine Systems, 2001. 28(3): p. 161-182
13. Cosoli, S., A. Mazzoldi, and M. Gačić, Validation of Surface Current Measurements in the Northern Adriatic Sea from High-Frequency Radars. Journal of Atmospheric and Oceanic Technology, 2010. 27(5): p. 908-919
14. Emery, B. and L. Washburn, Uncertainty Estimates for SeaSonde HF Radar Ocean Current Observations. Journal of Atmospheric and Oceanic Technology, 2019. 36(2): p. 231-247
15. Paduan, J.D. and L. Washburn, High-Frequency Radar Observations of Ocean Surface Currents. 2013. 5(Volume 5, 2013): p. 115-136
16. Lipa, B. and D.J.I.J.o.O.E. Barrick, Least-squares methods for the extraction of surface currents from CODAR crossed-loop data: Application at ARSLOE. IEEE Journal of Oceanic Engineering, 1983. 8(4): p. 226-253
17. Chapman, R.D. and H.C. Graber, Validation of HF Radar Measurements. Oceanography, 1997. 10(2): p. 76-79
18. Clementi, E., Aydogdu, A., Goglio, A. C., Pistoia, J., Escudier, R., Drudi, M., Grandi, A., Mariani, A., Lyubartsev, V., Lecci, R., Cretí, S., Coppini, G., Masina, S., & Pinardi, N., Mediterranean Sea Physical Analysis and Forecast (CMEMS MED-Currents, EAS6 system) (Version 1), C.M.E.M.S. (CMEMS). Editor. 2021
19. Taylor, K.E., Summarizing multiple aspects of model performance in a single diagram. Journal of Geophysical Research: Atmospheres, 2001. 106(D7): p. 7183-7192
20. Tian, Y., et al., Performance Metrics, Error Modeling, and Uncertainty Quantification. Monthly Weather Review, 2015. 144: p. 151209140733004
21. Nash, J.E. and J.V. Sutcliffe, River flow forecasting through conceptual models part I — A discussion of principles. Journal of Hydrology, 1970. 10(3): p. 282-290

22. Ardhuin, F., B. Chapron, and F. Collard, Observation of swell dissipation across oceans. Geophysical Research Letters, 2009. 36(6)
23. Sentchev, A. and M. Yaremchuk, VHF radar observations of surface currents off the northern Opal coast in the eastern English Channel. Continental Shelf Research, 2007. 27(19): p. 2449-2464

Appendix: August 2022 – August 2023 results summary

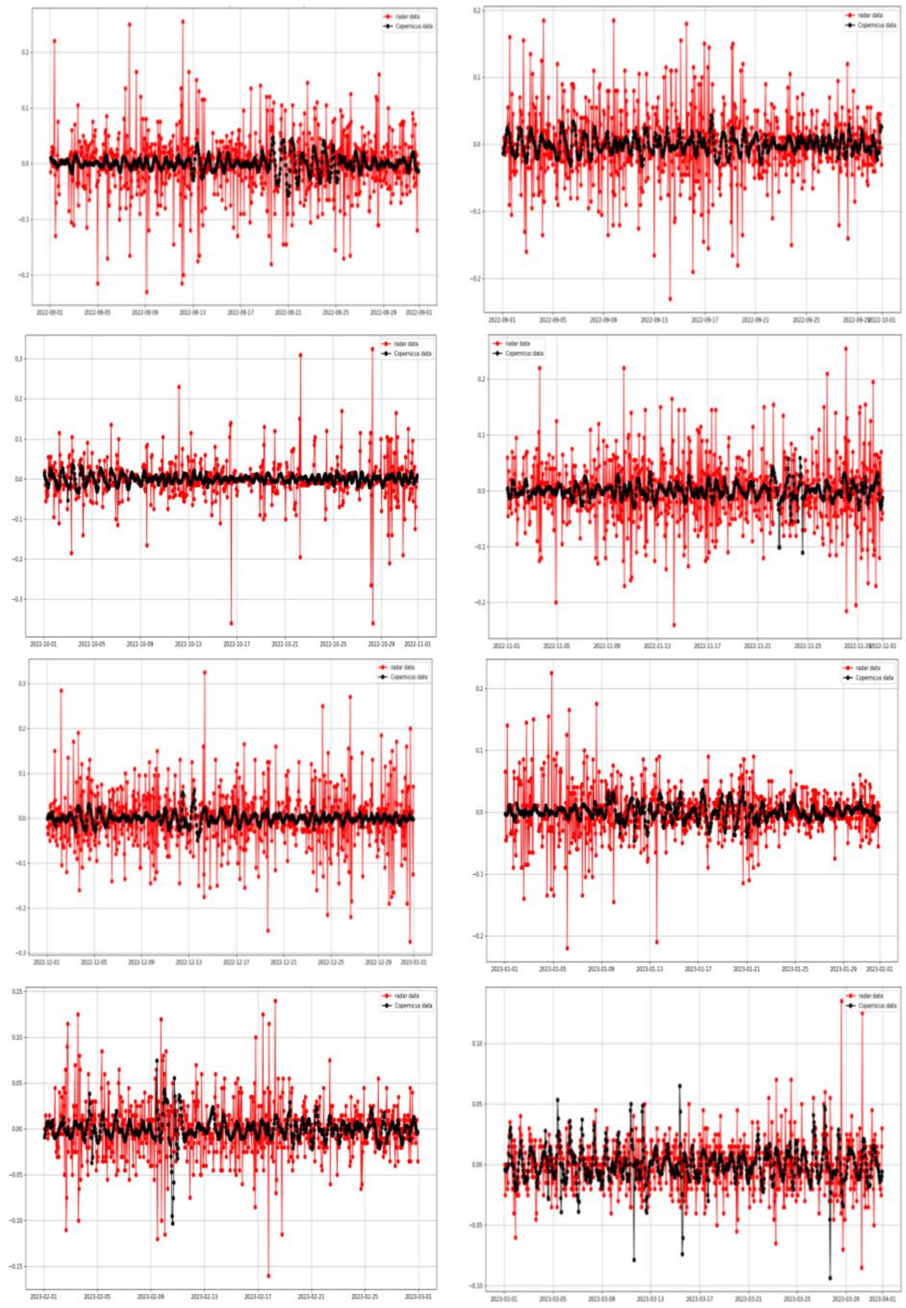

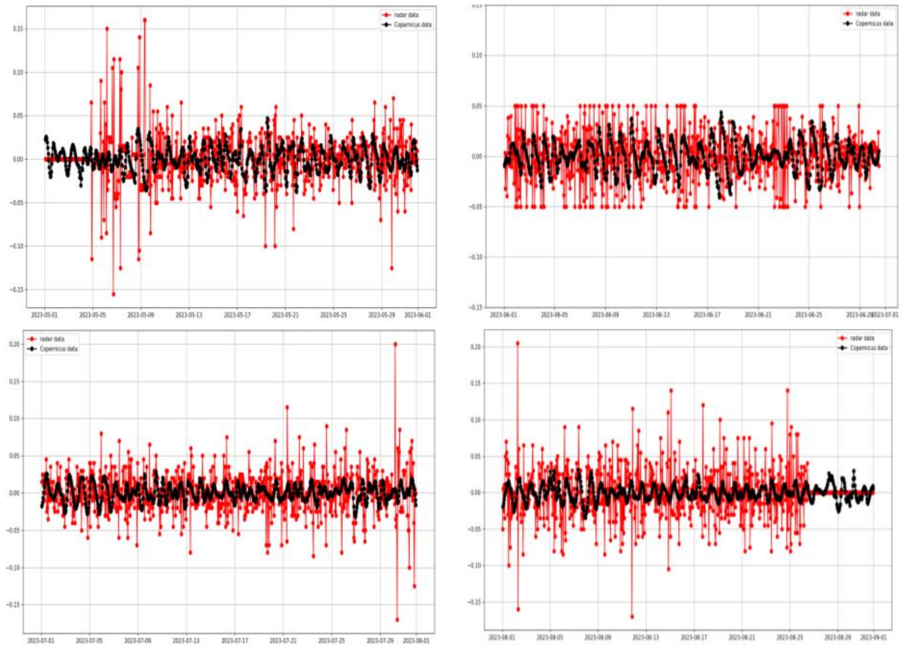

Fig. Ap1. Current speed temporal distribution from Radar HF data (red line) versus CMEMS Med MFC data (black line) for Point 1

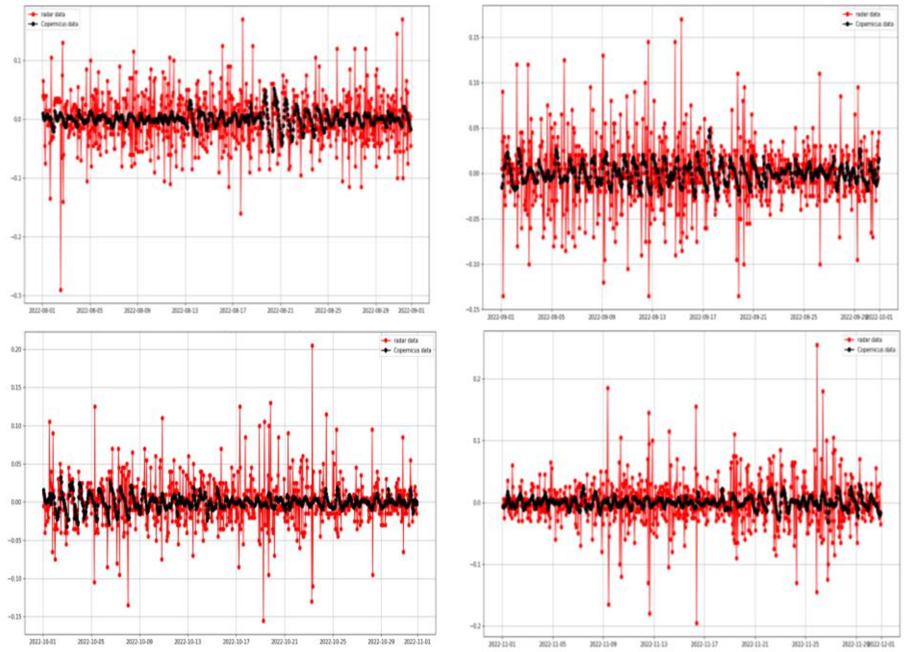

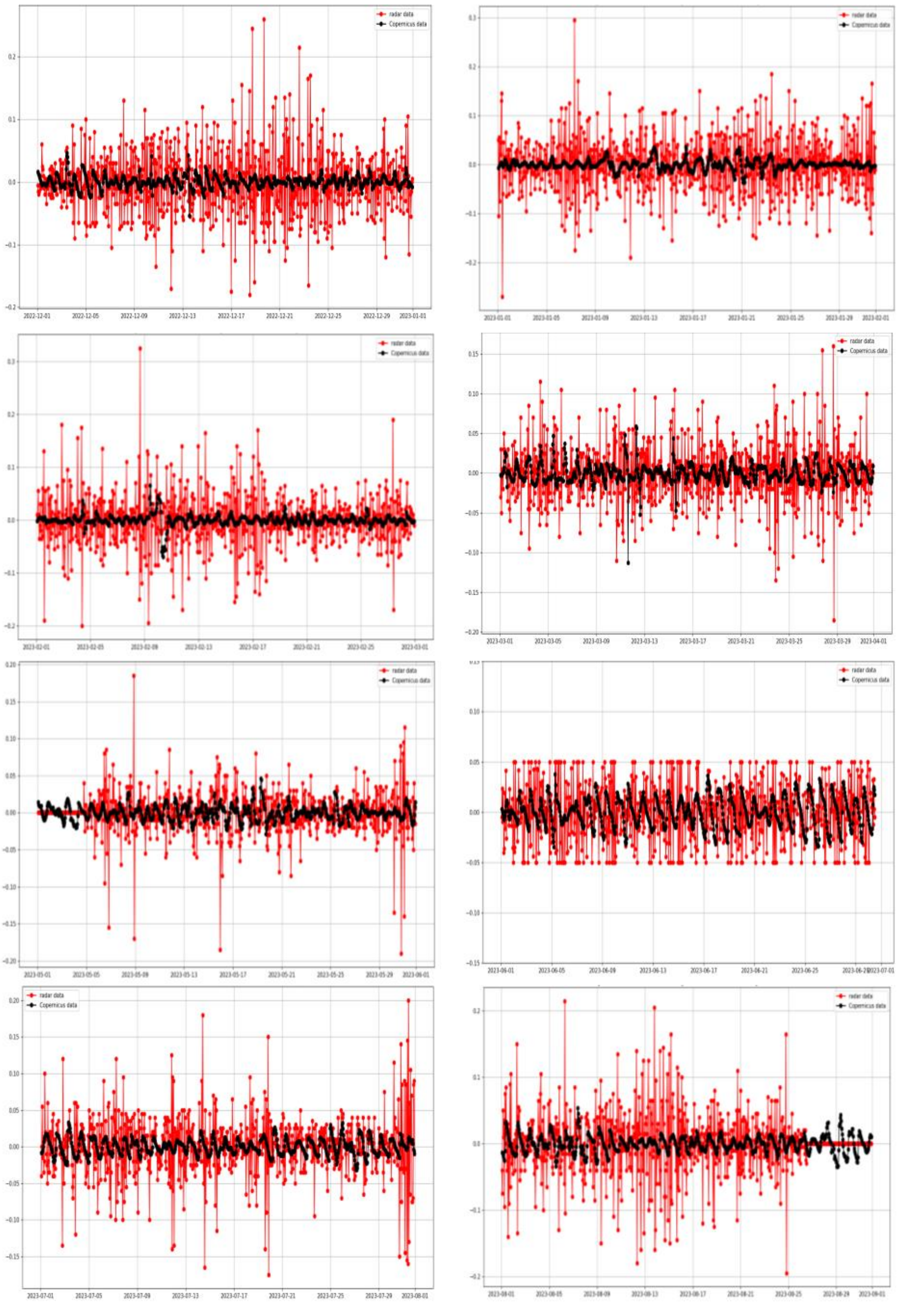

Fig. Ap2. Current speed temporal distribution from Radar HF data (red line) versus CMEMS Med MFC data (black line) for Point 2

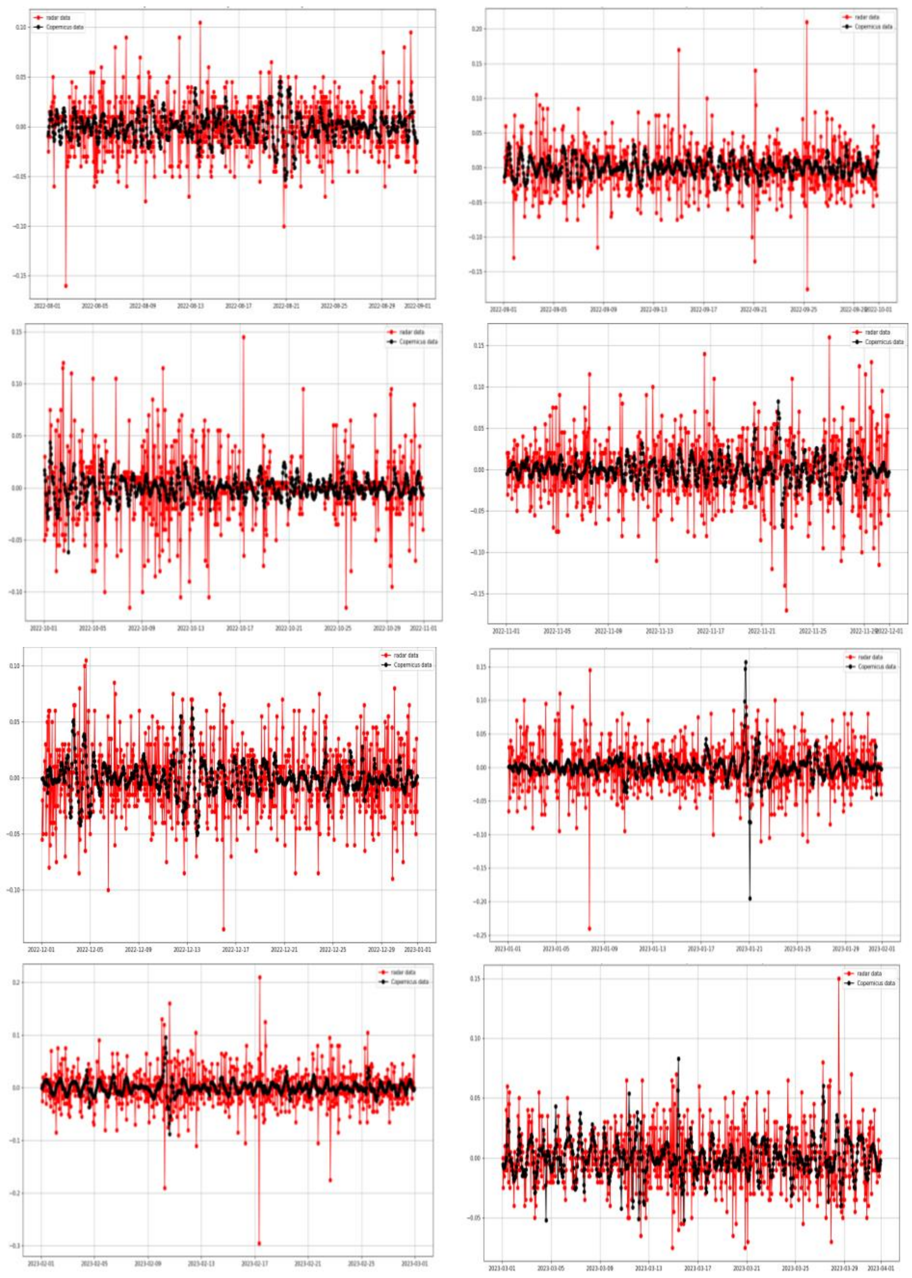
radar data
Copernicus data

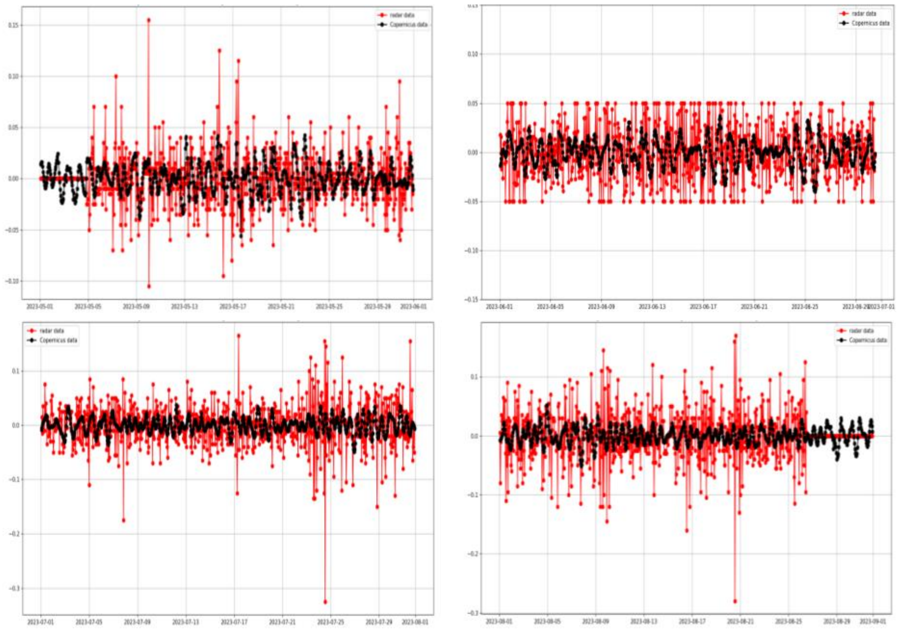

Fig. Ap3. Current speed temporal distribution from Radar HF data (red line) versus CMEMS Med MFC data (black line) for Point 3

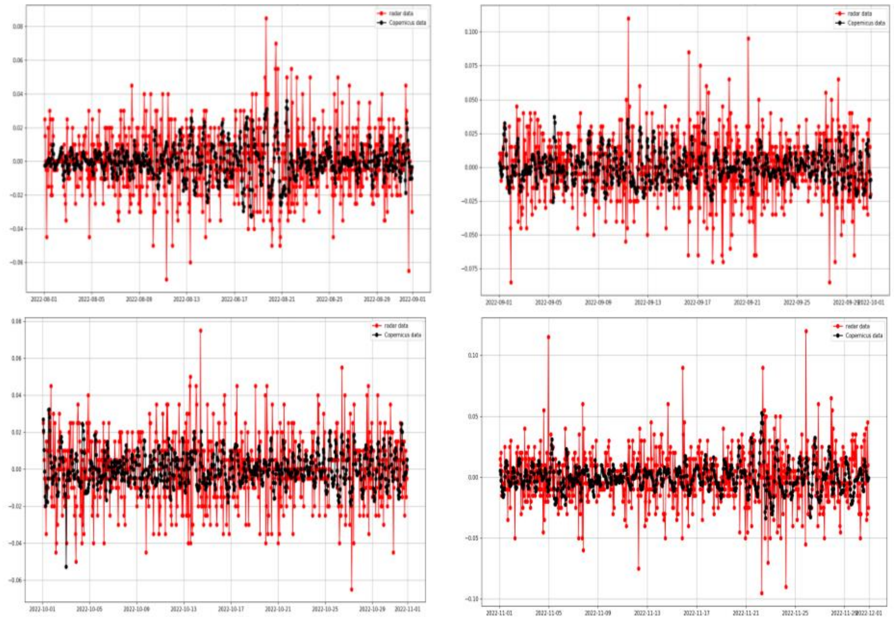

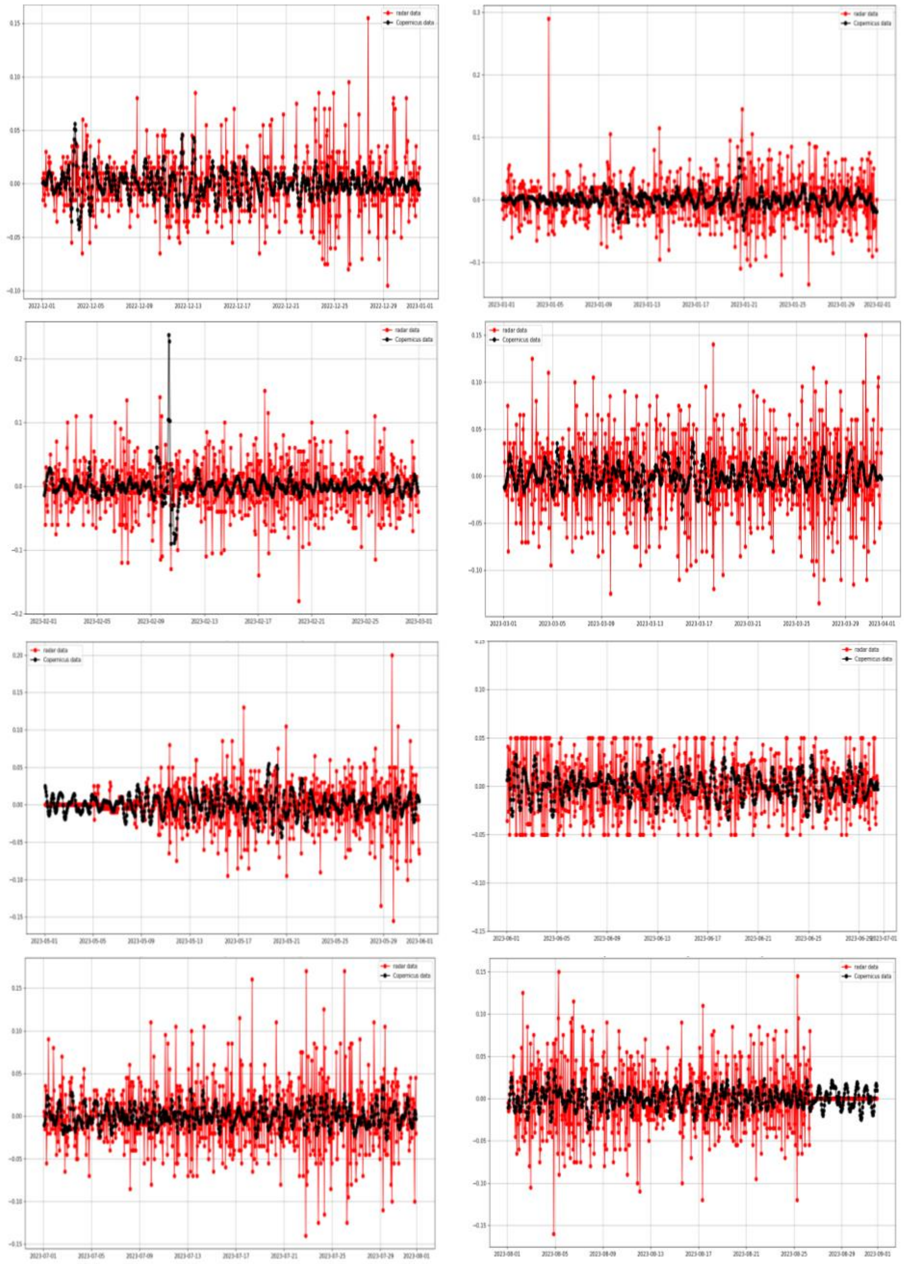

Fig. Ap4. Current speed temporal distribution from Radar HF data (red line) versus CMEMS Med MFC data (black line) for Point 4

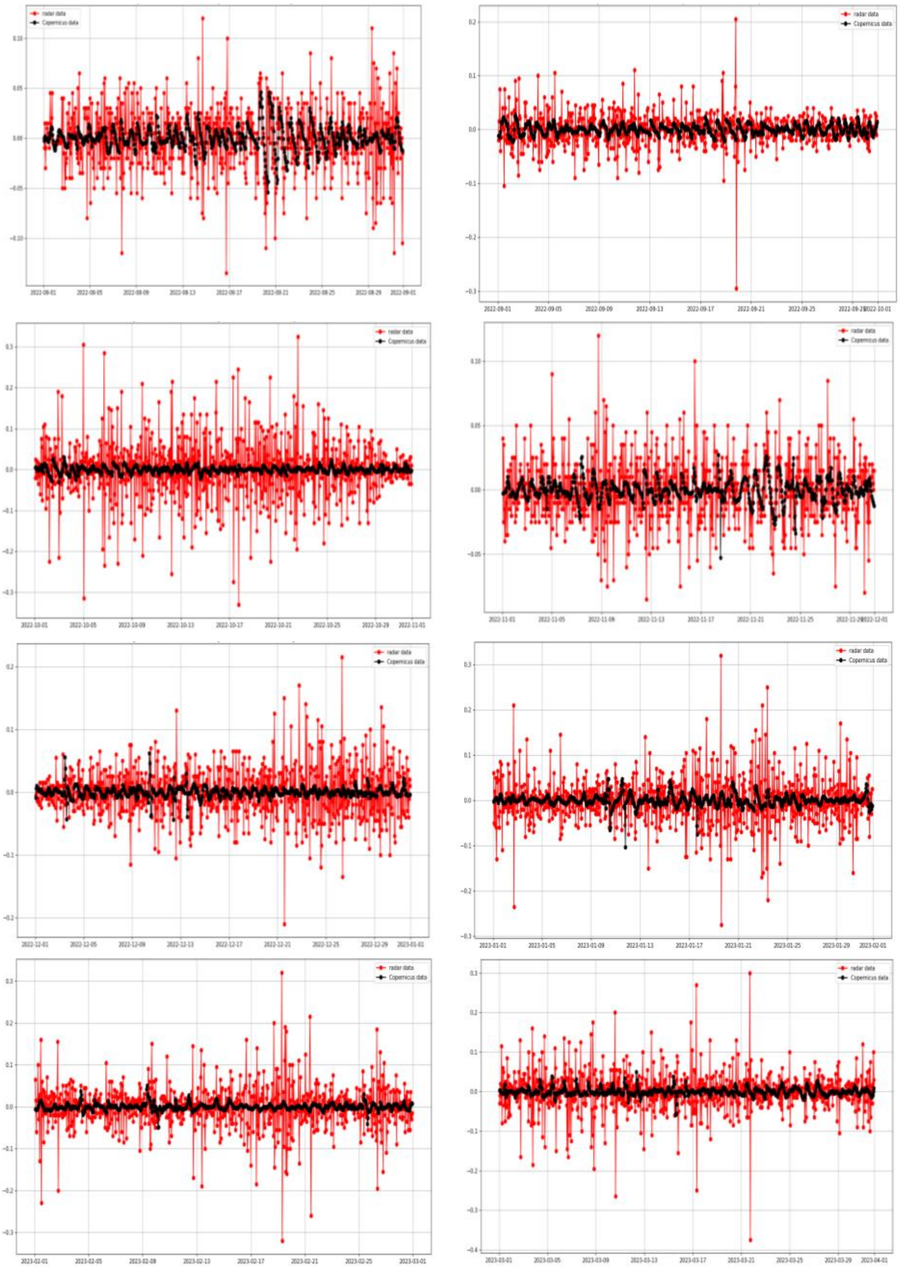
radar data
Copernicus data
2022-08-01
2022-09-01
2022-09-01
2022-10-01
2022-10-01
2022-11-01
2022-11-01
2022-12-01
2022-12-01
2023-01-01
2023-01-01
2023-02-01
2023-02-01
2023-03-01
2023-03-01
2023-04-01

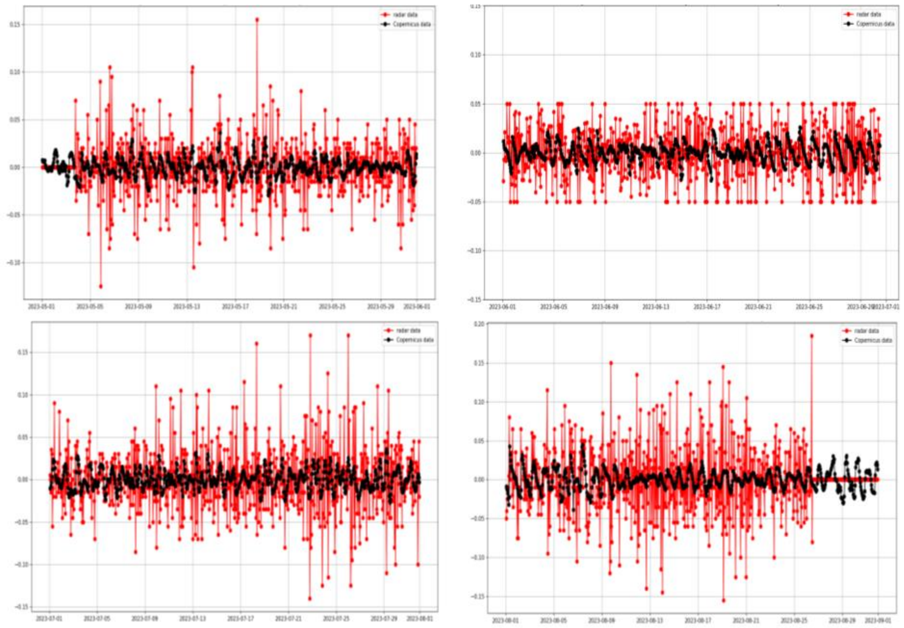

Fig. Ap5. Current speed temporal distribution from Radar HF data (red line) versus CMEMS Med MFC data (black line) for Point 5

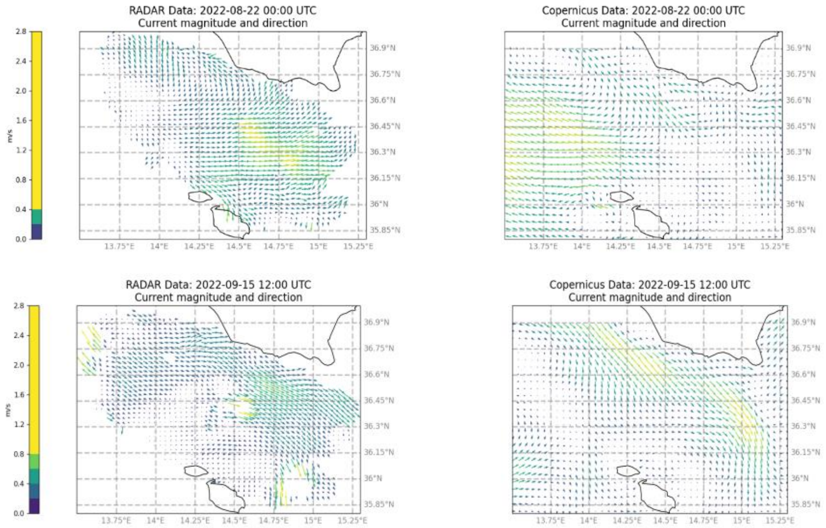

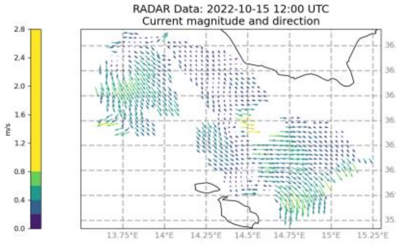
RADAR Data: 2022-10-15 12:00 UTC
Current magnitude and direction

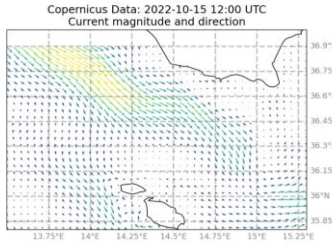
Copernicus Data: 2022-10-15 12:00 UTC
Current magnitude and direction

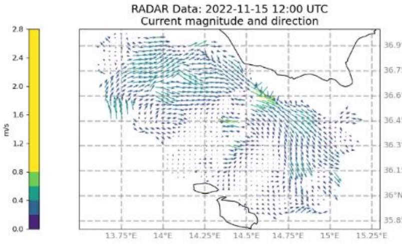
RADAR Data: 2022-11-15 12:00 UTC
Current magnitude and direction

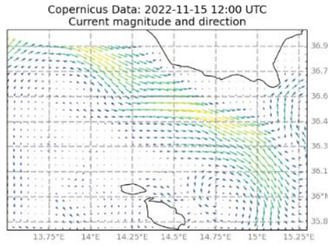
Copernicus Data: 2022-11-15 12:00 UTC
Current magnitude and direction

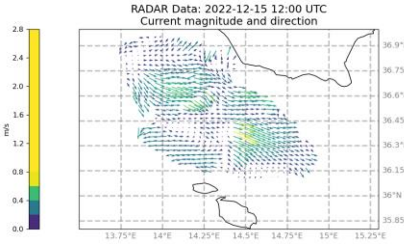
RADAR Data: 2022-12-15 12:00 UTC
Current magnitude and direction

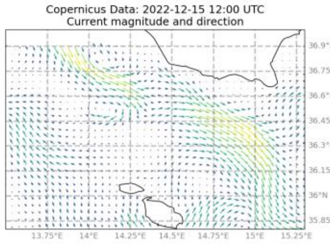
Copernicus Data: 2022-12-15 12:00 UTC
Current magnitude and direction

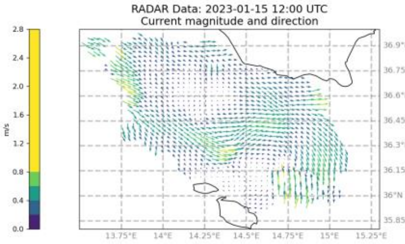
RADAR Data: 2023-01-15 12:00 UTC
Current magnitude and direction

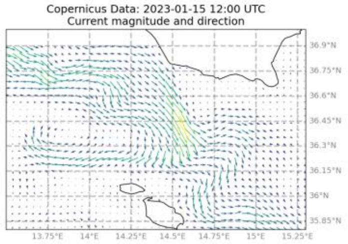
Copernicus Data: 2023-01-15 12:00 UTC
Current magnitude and direction

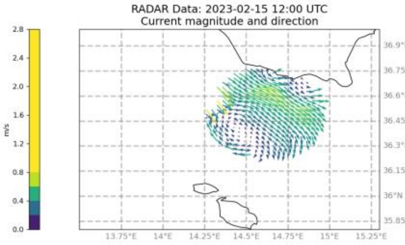
RADAR Data: 2023-02-15 12:00 UTC
Current magnitude and direction

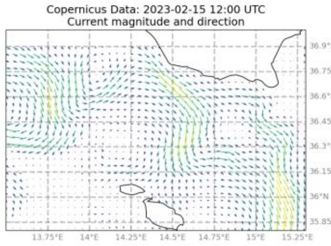
Copernicus Data: 2023-02-15 12:00 UTC
Current magnitude and direction

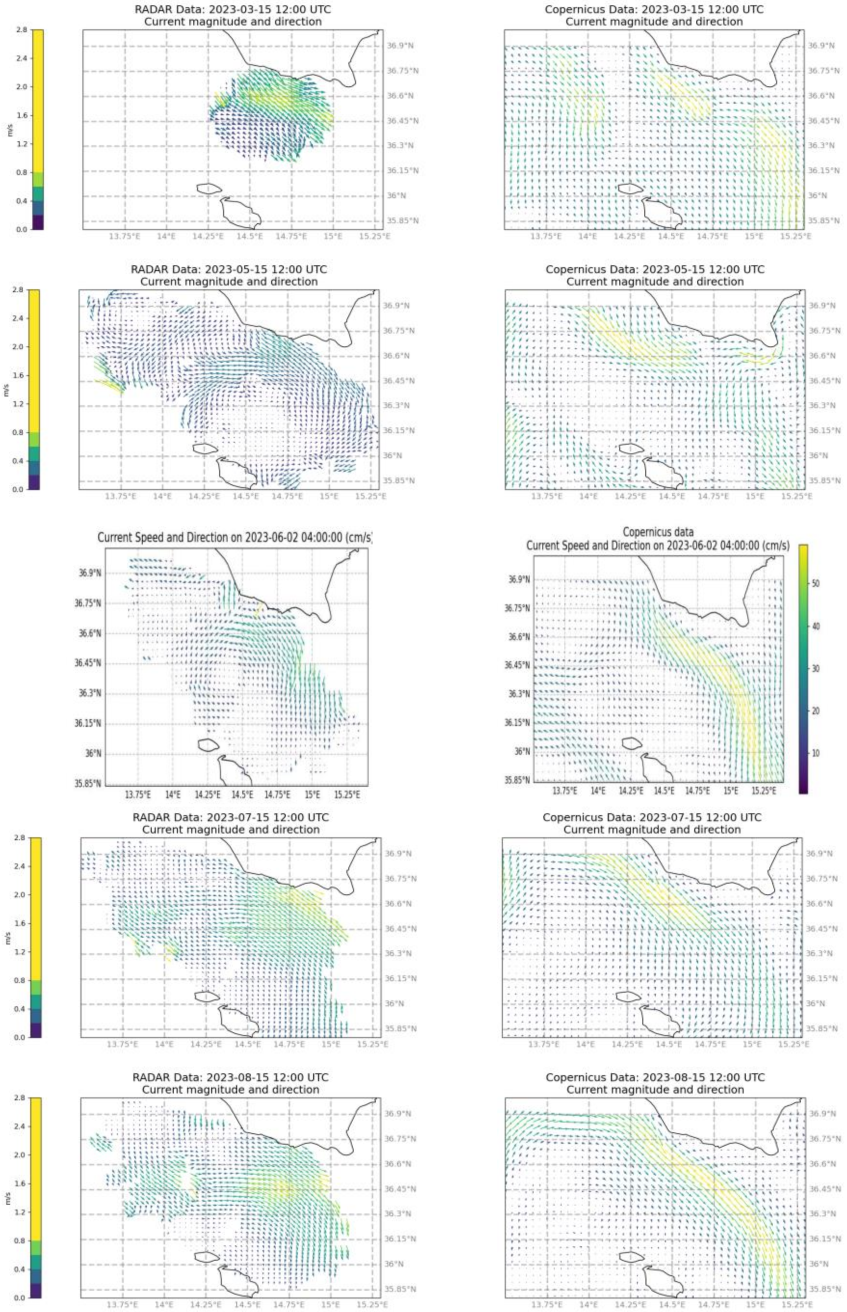

RADAR Data: 2023-03-15 12:00 UTC
Current magnitude and direction

Copernicus Data: 2023-03-15 12:00 UTC
Current magnitude and direction

RADAR Data: 2023-05-15 12:00 UTC
Current magnitude and direction

Copernicus Data: 2023-05-15 12:00 UTC
Current magnitude and direction

Current Speed and Direction on 2023-06-02 04:00:00 (cm/s)

Copernicus data
Current Speed and Direction on 2023-06-02 04:00:00 (cm/s)

RADAR Data: 2023-07-15 12:00 UTC
Current magnitude and direction

Copernicus Data: 2023-07-15 12:00 UTC
Current magnitude and direction

RADAR Data: 2023-08-15 12:00 UTC
Current magnitude and direction

Copernicus Data: 2023-08-15 12:00 UTC
Current magnitude and direction

Fig. Ap6. Characteristic spatial distribution of current speed and direction from Radar HF data (left) versus CMEMS Med MFC data (right) at specific time-points per month based on the entire spatial coverage of the HF radar (shown in Fig. 1). Horizontal units: Decimal degrees (WGS84)